The Astrophysical Journal, 805:120 (7pp), 2015 June 1 doi:10.1088/0004-637X/805/2/120

SPATIAL DISTRIBUTION OF X-RAY EMITTING EJECTA IN TYCHO'S SNR: INDICATIONS OF SHOCKED TITANIUM

M. Miceli[1,2], S. Sciortino[2], E. Troja[3,4], and S. Orlando[2]
[1] Dipartimento di Fisica & Chimica, Università di Palermo, Piazza del Parlamento 1, I-90134 Palermo, Italy; miceli@astropa.unipa.it
[2] INAF-Osservatorio Astronomico di Palermo, Piazza del Parlamento 1, I-90134 Palermo, Italy
[3] NASA, Goddard Space Flight Center, Greenbelt, MD 20771, USA
[4] Department of Physics and Department of Astronomy, University of Maryland, College Park, MD 20742, USA
Received 2015 January 27; accepted 2015 March 24; published 2015 May 27

ABSTRACT

Young supernova remnants (SNRs) show characteristic ejecta-dominated X-ray emission that allows us to probe the products of explosive nucleosynthesis processes and to ascertain important information about the physics of supernova explosions. Hard X-ray observations have recently revealed the presence of the radioactive decay lines of ^{44}Ti at ∼67.9 and ∼78.4 keV in Tycho's SNR. Here, we analyze a set of *XMM-Newton* archive observations of Tycho's SNR. We produce equivalent width (EW) maps of the Fe K and Ca XIX emission lines and find indications for a stratification of the abundances of these elements and significant anisotropies. We then perform spatially resolved spectral analysis by identifying five different regions characterized by high/low values of the Fe K EW. We find that the spatial distribution of the Fe K emission is correlated with that of Cr XXII. We also detect the Ti K line complex in the spectra extracted from the two regions with the highest values of Fe and Cr EWs. The Ti line emission remains undetected in regions where Fe and Cr EWs are low. Our results indicate that the post-shock Ti is spatially colocated with other iron-peak nuclei in Tycho's SNR, in agreement with the predictions of multi-D models of SNe Ia.

Key words: ISM: individual objects (Tycho's SNR) – ISM: supernova remnants – X-rays: ISM

1. INTRODUCTION

Supernova remnants (SNRs) govern the physical and chemical evolution of our Galaxy. An exploding star releases $\sim 10^{51}$ erg of kinetic energy through solar masses of ejecta which expand supersonically and drive powerful shocks back and forth in the ambient medium and in the ejecta themselves. The X-ray emission from young SNRs is a powerful diagnostic tool to study the imprint of the supernova explosion on the evolution of the remnant. The X-ray emission of young SNRs is, in fact, ejecta-dominated, being mainly associated with the metal-rich material expelled in the supernova explosion and heated to X-ray emitting temperatures by the interaction with the reverse shock. The ejecta carry information about explosive nucleosynthesis processes and can "keep memory" of the physics of the explosion itself (e.g., Badenes et al. 2008b; Miceli et al. 2006).

In particular, the iron-group elements (e.g., Cr, Mn, Ti, together with Fe and Ni) are synthesized in the inner layers of the exploding star and can provide important information concerning the progenitor (Badenes et al. 2008a; Yamaguchi et al. 2014). It has been shown that there is a correlation in the centroids of the X-ray line complexes of Cr, Mn, and Fe in a large number of SNRs, including Kepler, W49B, N103B, Tycho, G344.7–0.1, and Cas A (Yang et al. 2013). This result seems to suggest that these elements are spatially colocated in the explosions in this large sample of SNRs, which includes both core-collapse and Type Ia SNRs. On the other hand, it has recently been shown that the spatial distribution of ^{44}Ti is significantly different from that of Fe in the Cassiopeia A SNR (Grefenstette et al. 2014). However, the radioactive emission traces the entire amount of Ti, concentrated in the unshocked interior of the remnant, while the X-ray emission from Fe originates only from the ejecta shocked by the reverse shock. Therefore, the different morphologies may be due to the fact that we only observe a small fraction of Fe in X-rays.

The radioactive hard X-ray signature of ^{44}Ti (whose radioactive decay lines are at 67.86 and 78.36 keV) has recently been observed in Tycho's SNR through the analysis of *Swift*/BAT (Troja et al. 2014) and *INTEGRAL* (Wang & Li 2014) observations. Tycho's SNR is the remnant of an SN Ia explosion (Badenes et al. 2006; Krause et al. 2008) that occurred in 1572 AD and presents clear signatures of efficient particle acceleration (see, e.g., Bykov et al. 2011; Eriksen et al. 2011; Morlino & Caprioli 2012; Slane et al. 2014). Besides regions characterized by strong synchrotron X-ray emission, its thermal X-ray radiation is dominated by the ejecta (Cassam-Chenaï et al. 2007).

In Type Ia SNRs, delayed-detonation models (e.g., Gamezo et al. 2005) predict that Fe-group elements are located in the inner parts of the ejecta profile, surrounded by intermediate-mass elements (e.g., Si, S, and Ca). More recently, three-dimensional delayed-detonation models developed by Seitenzahl et al. (2013) revealed details of the element stratification by showing that Fe-group elements can have velocities higher than those of ^{56}Ni (which, after the decay, produces the bulk of Fe-rich ejecta), but still lower than those of the intermediate-mass elements, which are then expected to expand in an outer shell. Three-dimensional deflagration models (e.g., Röpke and Hillebrandt 2005) generally suggest more efficient mixing in the abundances distribution than classical 1D deflagration models (Nomoto et al. 1984).

Here, we take advantage of the deep set of *XMM-Newton* archive observations of Tycho's SNR to study the spatial distribution of the heavy elements in the shocked ejecta. We also look for the Ti K emission line complex at ∼4.9 keV to check whether or not the spatial distribution of the shocked Ti somehow correlates with that of the shocked Fe-rich ejecta

and of the other Fe-group elements. The Ti K line has not yet been observed in any SNRs; only a few indications of the Ti Heα emission line in the *ASCA* spectrum of W49B have been reported (Hwang et al. 2000), although this was not confirmed by subsequent *XMM-Newton* observations (Miceli et al. 2006).

2. RESULTS

We analyzed the archive *XMM-Newton* EPIC observations 0096210101, 0310590101, 0310590201, 0412380101, 0412380201, 0412380301, 0412380401, 0511180101, all with pointing coordinates $\alpha_{J2000} = 00^{h}25^{m}22\overset{s}{.}0$, $\delta_{J2000} = +64°08'24\overset{''}{.}0$. Data were processed using the Science Analysis System (SAS V12). We selected events with PATTERN $\leqslant 12$ for the MOS cameras, PATTERN $\leqslant 4$ for the pn camera, and FLAG = 0 for both. We inspected all of the light curves and adopted the ESPFILT task (which is based on a σ-clipping algorithm) to remove high background periods from the event lists, thus filtering out the contribution from the flaring background associated with soft protons. We obtained a total screened exposure time for the pn observations of 124.9 ks. Event files were processed with the EVIGWEIGHT task to correct for vignetting effects. Images were produced by adopting the procedure described in Miceli et al. (2006, see their Section 2). Spectral analysis was performed in the energy band 3.6–6.7 keV using XSPEC V12.8.2. This band was chosen so as to include the Ti K line and the characteristic X-ray line emission from other Fe-group elements (Cr, Mn, and Fe). We also carefully modeled the bright Ca emission to study the intermediate-mass elements and to account for faint Ca XIX and Ca XX transitions, which have energies of ~4.9 keV and may contribute to the flux in the energy band where we expect to find the Ti K lines. The pn spectra of all the different observations were fitted simultaneously. For each spectrum, we subtracted the background spectrum extracted from a nearby region immediately outside of the SNR shell and we verified that the best-fit values do not depend significantly on the choice of the background region. In all of the fittings, the column density of the interstellar absorption was fixed to $N_H = 7 \times 10^{21}$ cm^{-2} in agreement with Cassam-Chenaï et al. (2007). Small local variations of N_H can be present across the remnant (Slane et al. 2014), but we do not expect this to have any significant effects on our results given the relatively hard energy band considered here.

2.1. Image Analysis

To trace the spatial distribution of the chemical abundances in the shocked ejecta, we produced equivalent width (EW) maps. X-ray line and continuum emission both scale with the plasma emission measure, and EW maps allow us to disentangle higher element abundances from higher emission measures. Although the EW of an emission line increases with the element abundance, it also varies with the plasma temperature and ionization age (e.g., van Paradijs & Bleeker 1999). Therefore, EW maps provide indications of the distribution of the abundances, but do not provide quantitative information and need to be tested with spatially resolved spectral analyses (as in Section 2.2).

To identify the Fe-group elements, we produced the EW map for the Fe K line complex, which, thanks to the high statistics of the *XMM-Newton* data, has a much higher signal-to-noise ratio than that presented in Hwang et al. (2002). We also produce, for the first time, the EW map of the Ca XIX emission lines and, for comparison, of the Si XIII lines. To produce these maps, we divided the continuum-subtracted line images (in the 1.65–2.05 keV, 3.6–4.05 keV, and 6.1–6.7 keV energy bands for Si, Ca, and Fe, respectively) by the corresponding underlying continuum. The underlying continuum was estimated by modeling the global[5] pn spectrum of the remnant in a continuum band adjacent to the line emission with a phenomenological power-law model. In particular, we considered the 4.4–6.1 keV band for Ca and Fe (with best-fit photon index $\Gamma = 2.6$), and the 1.47–1.65 keV band for the Si line (in this case, with a best-fit $\Gamma = 1.65$). Although spatial variations of the spectral slope over the SNR may locally affect these maps, our spatially resolved spectral analysis shows that the EW maps provide reliable results (see Section 2.2).

Figure 1 shows the continuum (4.4–6.1 keV) count-rate image of Tycho's SNR, together with the Si, Ca, and Fe EW maps. While the Si EW is fairly distributed over the whole remnant (in agreement with the Si EW map obtained with *Chandra* by Hwang et al. 2002), our Fe and Ca EW maps reveal strong anisotropies with high values in the north and relatively low values in the center and elsewhere in the rim. It is not easy to ascertain the origin of these inhomogeneities, which may be intrinsic or result from the interaction of the remnant with the ambient medium. In fact, Tycho's SNR evolves in a structured environment (see, e.g., Chiotellis et al. 2013; Williams et al. 2013) which may produce anisotropies and corrugations in the reverse shock front. On the other hand, these anisotropies are not present in the Si-rich ejecta, and therefore the observed Ca and Fe inhomogeneities may be intrinsic in the ejecta structure.

The Ca XIX EW presents a bright arc immediately behind the northern border of the shell (region 4 in Figure 1). A large region characterized by a strong Fe EW is clearly present behind this bright Ca arc, closer to the center of the remnant (region 1 in Figure 1). Figure 2 shows the comparison between the Ca and Fe EWs (and the continuum emission) to highlight the differences in the distribution of these elements. The spatial distribution of the Si, Ca, and Fe EWs is suggestive of a possible stratification of the SN ejecta, with Fe confined within the inner region and the lower-Z elements forming an outer envelope. An indirect spectroscopic indication of stratification between Fe-rich ejecta and lighter elements was proposed on the basis of the analysis of the global spectrum of the remnant (e.g., Hwang et al. 1998) and of the spectrum extracted from a large region in the eastern part of the shell (Badenes et al. 2006). However, with our EW map (together with the spatially resolved spectral analysis presented in Section 2.2), we can directly separate out the different elements spatially, thus revealing that besides the element stratification, there are also strong anisotropies in the Ca and Fe distributions.

A stratification in the ejecta abundances is predicted by 3D simulations of delayed-detonation SNe Ia, which show a turbulent inner region characterized by iron-group elements surrounded by a smooth distribution of intermediate-mass elements (including Ca) in the outer layers of the ejecta (Kasen et al. 2009). This stratification between Fe and Ca is also observed in SNe Ia (e.g., Tanaka et al. 2011). As for the inhomogeneities in the Ca map, the light-echo spectrum of

[5] To exclude the contribution of the synchrotron emitting limbs, we extracted the spectrum from a circular region slightly smaller than the shell.

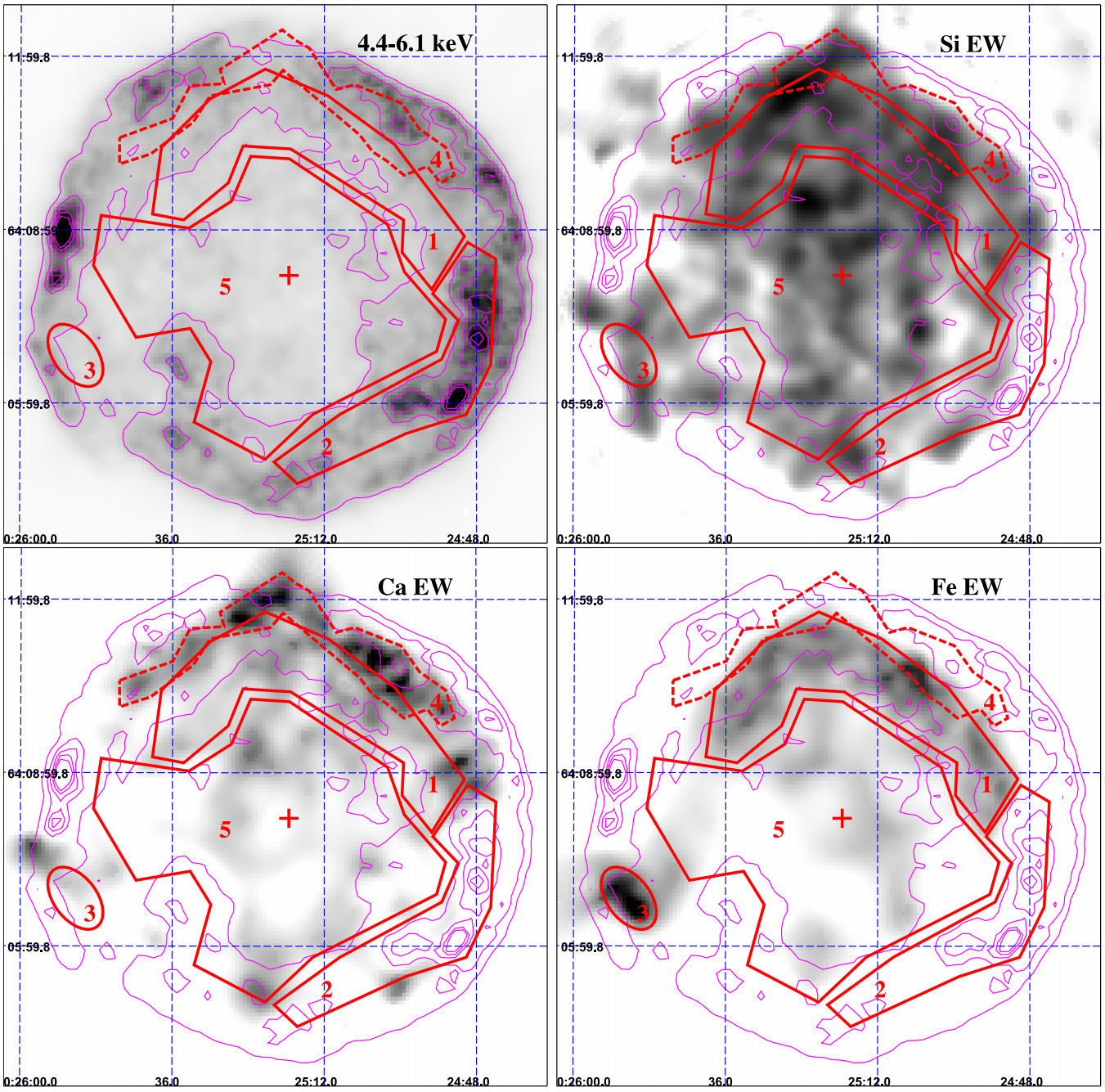

Figure 1. Upper left panel: EPIC count-rate images (MOS and pn mosaic) of Tycho's SNR in the continuum band 4.4–6,1 keV. Upper right panel: Si EW map obtained in the 1.65–2.05 keV band. Lower left panel: Ca EW map obtained in the 3.6–4.05 keV band. Lower right panel: the Fe K EW map obtained in the 6.1–6.7 keV band. The bin size is 4″ and the images are all adaptively smoothed to a signal-to-noise ratio $R = 10$, except for the Si EW map where $R = 25$. We superimposed the regions selected for the spectral analysis (in red) together with the contour levels of the continuum image at 10%, 20%, 30%, 40%, and 50% of the maximum (in magenta). The cross marks the position chosen as the center of the shell. North is up and east is to the left.

Tycho's SN has revealed a high-velocity component in the Ca-rich ejecta (Krause et al. 2008). Also, the presence of fast Ca-rich knots deduced by Krause et al. (2008) may explain why the Ca EW presents a much higher level of anisotropy than the Si EW. Our results then suggest that the remnant has retained the memory of the pristine ejecta distribution.

We also confirm the presence of the bright Fe-rich eastern knot to the southeast (Vancura et al. 1995). Our map shows that this knot (region 3 in Figure 1) has the highest Fe K EW observed in the whole remnant (see also Section 2.2 and Figure 4). We find that the projected distance between this knot and the approximate center of the remnant (indicated by a cross in Figure 1) is 30% higher than that of region 1 (i.e., of the "smooth" distribution of shocked Fe-rich ejecta). This difference can be explained by considering the Fe-rich knot as moderately overdense shrapnel (a density inhomogeneity in the ejecta profile) that moves beyond the Fe-rich ejecta shell, as modeled by Miceli et al. (2013). Ejecta shrapnels are common in core-collapse SNRs, but localized clumps of ejecta have also been observed in SNe Ia and their evolution has been modeled

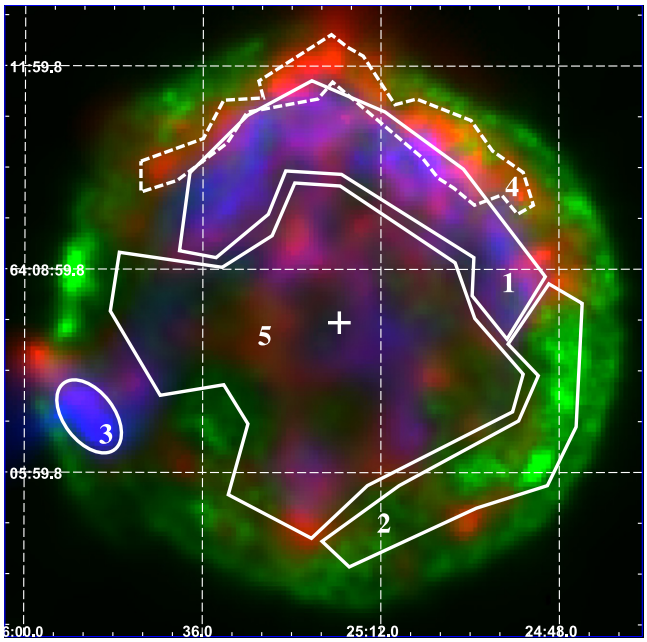

Figure 2. Color–composite image showing the EPIC count-rate images in the 4.4–6,1 keV band (green), together with the Ca EW map (in red) and the Fe K EW map (in blue). The regions selected for the spectral analysis are superimposed.

with hydrodynamic simulations (Wang et al. 2003, 2006; Orlando et al. 2012), and so we can argue that the eastern knot traces an ejecta clump originating in the inner layers of the exploding progenitor star.

2.2. Spectral Analysis

We performed a spatially resolved spectral analysis by selecting five regions defined on the basis of the Ca and Fe EW maps and shown in Figures 1 and 2. Regions 1 and 3 are very bright in the Fe K EW map and are expected to be Fe-rich; region 2 traces a part of the shell characterized by a bright continuum and low EW for both Ca and Fe; region 4 is where the Ca EW is highest; while region 5 shows low values of the continuum and of the EW of Fe and Ca.

Figure 3 shows the pn spectrum of region 1 obtained by summing all of the observations (the analysis has been performed simultaneously on all the different spectra; we show the summed spectrum only for visibility reasons). We found that in this spectrum and in all the other spectra, both the Ca and the Fe line complexes are significantly broadened with the Ca clearly showing a double-peaked feature. We interpret this broadening as an effect of the superposition of different conditions in the ionization states of the plasma and we model the spectra with two thermal components of optically thin plasma in non-equilibrium ionization (VNEI model in XSPEC) with different temperatures, abundances, and ionization time-scales, τ (this model describes the spectra significantly better than a single-temperature model). We associate the low τ component with the ejecta closer to the reverse shock and the high τ component with the material shocked at earlier stages, i.e., the ejecta at higher distances from the center of the shell. For each component, we only allow the Ca and Fe abundances to be free to vary and we impose solar abundances for all other elements (except for Ni, which is assumed to have the same

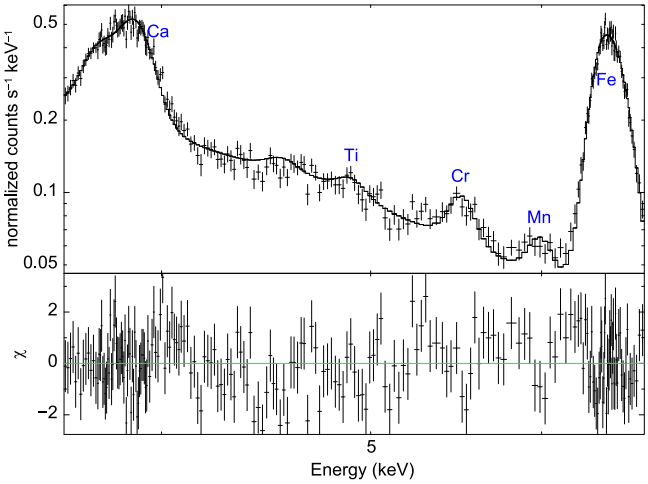

Figure 3. Summed pn spectrum extracted from region 1 of Figure 1, together with its best-fit model and residuals. The elements contributing to the emission lines described in the text are labeled in blue.

abundance as Fe). We also add three Gaussian components to model the line emission from shocked Ti (if any), Cr, and Mn.

Table 1 shows the best-fit parameters for the five spectral regions. The temperatures of the low τ component (labeled "1") are significantly lower than those of the high τ component. This result suggests that the temperature of the electrons increases as they move away from the reverse shock, in agreement with what is expected in the case of electron heating by Coulomb collisions with hotter protons in the post-shock flow.

Although the Ca and Fe abundances in the low τ component are poorly constrained, the abundances in the high τ component show much smaller errors. This is because the high τ component dominates the flux in the line bands in all of the regions, being in the range ~63%–74% of the total in the 3.6–4.05 keV band and 65%–85% of the total in the 6.1–6.7 keV band. The pattern of the best-fit abundances shows that the features observed in the EW maps of Figure 1 are indeed the results of variations in the plasma chemical composition. In particular, region 2 and region 5, characterized by low values of both Ca and Fe EW, show the minimum values of the abundances Ca_2 and Fe_2 (see Table 1). Also, the Fe EW, measured from the spectral analysis in regions 1–5 (shown in Figure 4), remarkably confirms the results of the EW maps.

Table 1 shows the presence of the Cr and Mn emission lines, whose line centroids are in good agreement with those found by Tamagawa et al. (2009) in the *Suzaku* global spectrum of the remnant. Our spatially resolved spectral analysis allows us to find spatial variations in the intensity of these lines. We measured the EW of the Cr and Mn emission lines in all of the regions. While the Mn EW presents large error bars, we reveal significant variations in the EW of the Cr XXII line. Figure 4 shows that the Cr EW derived by our fittings increases in regions with high Fe EW. This correlation strongly indicates that Fe and Cr are spatially colocated, thus confirming what was proposed by Yang et al. (2013) on the basis of the global spectrum of the remnant.

We also found that the quality of the fits in regions 1 and 3 improves significantly by adding to the model a Gaussian component with energy $E \sim 4.90$ keV, corresponding to some

Table 1
Results of the Spectral Analysis for the Regions Shown in Figure 1

Parameter	Region 1	Region 2	Region 3	Region 4	Region 5
kT_1 (keV)	$1.45^{+0.2}_{-0.07}$	$1.37^{+0.6}_{-0.15}$	$1.5^{+1.1}_{-0.2}$	1.2 ± 0.1	$1.3^{+0.4}_{-0.2}$
τ_1 (10^9 s cm^{-3})	3.2 ± 0.7	3.6 ± 1.4	$7^{+3}_{-2.}$	3.0 ± 1.0	0.6 ± 0.3
EM_1[a] (10^{18} cm^{-5})	9^{+19}_{-3}	29^{+25}_{-14}	9^{+22}_{-7}	24^{+40}_{-6}	$13^{+0.6}_{-0.5}$
Ca_1	500 ± 300	200 ± 140	600 ± 500	600 ± 400	140^{+40}_{-90}
Fe_1	300 ± 200	70 ± 60	200 ± 150	200 ± 160	300 ± 250
kT_2 (keV)	4.3 ± 0.8	5.0 ± 0.9	4.0 ± 1.6	$3.3^{+1.1}_{-0.4}$	5.0 ± 0.4
τ_2 (10^9 s cm^{-3})	26 ± 2	23 ± 3	33^{+18}_{-4}	27^{+3}_{-4}	$25.5^{+1.2}_{-1.0}$
EM_2[a] (10^{18}cm^{-5})	8 ± 2	33^{+3}_{-4}	$2.5^{+4}_{-1.4}$	13 ± 3	$10.0^{+0.6}_{-0.9}$
Ca_2	21^{+8}_{-4}	$5.3^{+1.3}_{-1.1}$	36^{+13}_{-19}	37^{+4}_{-7}	7.4 ± 0.7
Fe_2	21^{+9}_{-4}	$2.3^{+0.4}_{-0.3}$	30^{+30}_{-18}	28 ± 10	5.4 ± 0.4
E_{Ti} (keV)	$4.90^{0.05}_{-0.04}$	4.9[b]	4.93 ± 0.06	4.9[b]	4.9[b]
N_{Ti} (10^{-6} cm^{-2} s^{-1})	2.1 ± 1.2	0(<0.6)	0.5 ± 0.3	$0.8^{+0.9}_{-0.8}$	0(<0.5)
E_{Cr} (keV)	$5.50^{+0.02}_{-0.03}$	5.52 ± 0.15	$5.52^{+0.05}_{-0.04}$	$5.51^{+0.04}_{-0.02}$	5.47 ± 0.08
N_{Cr} (10^{-6} cm^{-2} s^{-1})	6.3 ± 1.1	2.3 ± 1.2	$0.8^{+0.4}_{-0.3}$	3.9 ± 0.9	$6.1^{+1.5}_{-1.6}$
E_{Mn} (keV)	6.02 ± 0.03	$6.04^{+0.04}_{-0.06}$	6.1[b]	6.00 ± 0.06	6.05 ± 0.08
N_{Mn} (10^{-6}cm^{-2} s^{-1})	$3.8^{+1.0}_{-1.1}$	2.0 ± 1.1	0.3 ± 0.3	2.8 ± 0.8	$2.8^{+1.3}_{-1.5}$
Reduced χ^2 (dof)	1.05 (1855)	0.97 (2022)	1.01 (203)	0.98 (1399)	1.07 (2521)

Note. All errors are at the 90% confidence level.
[a] Emission measure per unit area.
[b] Unconstrained.

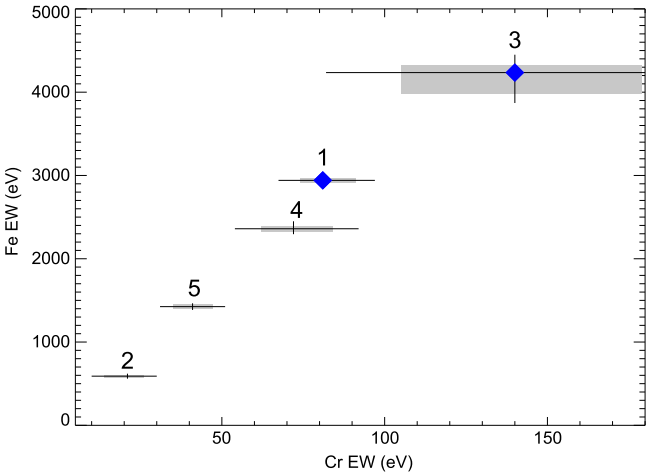

Figure 4. Fe EW in the 6.1–6.7 keV energy band vs. Cr XXII EW in the 5.3–5.7 keV band as obtained from the spatially resolved spectral analysis of the spectra extracted from the regions shown in Figure 1. Error bars are the 68% (gray boxes) and 90% (black crosses) confidence levels. The blue diamonds mark the regions where we detected the Ti emission line.

transitions to the ground level of Ti (Kramida et al. 2014). The normalization of this component is higher than zero at almost 3σ ($\Delta\chi^2 \sim 8$) in region 1 and at more than 2σ in region 3 ($\Delta\chi^2 \sim 5$). Although this additional Ti line only affects a few bins of the spectra, it still produces a significant reduction in the χ^2 (which is calculated in the broad 3.6–6.7 keV energy band), thus indicating that the improvement of the fits in the Ti energy band is large indeed. Figure 3 shows that the Ti emission line is visible when considering the summed (over all the observations) spectrum of region 1. Interestingly, we detect significant Ti emission only in those regions with the highest Fe K and Cr EWs (see Figure 4). In regions 2 and 5 (where the Fe and Cr EWs are the lowest), the best-fit value of the normalization of the Ti line is zero. We observe only a marginal ($\sim 1.5\sigma$) indication for the Ti line in region 4. We checked our results by analyzing also the *Chandra* ACIS spectra of region 1 extracted from observations 10093-97, 10902-4, and 10906 (all performed in 2009, for a total of 734 ks).[6] The combined fits of the pn and ACIS spectra are reasonably good (reduced $\chi^2 = 1.26$ with 3644 degrees of freedom (dof)), although it presents clear residuals corresponding to the Ca and Fe line complexes, possibly associated with the different PSFs of the two telescopes (a larger contamination from bright nearby regions is expected in the *XMM-Newton* spectra). These residuals make the Ti line unconstrained, and so we focus on the 4.4–6.1 keV continuum band by freezing all of the parameters, except the normalization of the Gaussian components, to the best-fit values obtained in 3.6–6.7 keV. We obtain a reduced $\chi^2 = 1.06$ with 1626 dof, and the normalization of the Ti line is $N_{Ti} = 1.4^{+0.8}_{-0.7} \times 10^{-6}$ cm^{-2} s^{-1}, in agreement with the value in Table 1. Also, $N_{Ti} > 0$ at more than 3σ.

3. DISCUSSION AND CONCLUSIONS

We analyzed several archive *XMM-Newton* observations of Tycho's SNR to study the spatial distribution of the shocked ejecta. We found strong indications for anisotropies in the distributions of Fe-rich and Ca-rich shocked ejecta, which appear to be mainly localized in the northern part of the remnant. We also found a radial stratification of the ejecta chemical composition, with Ca and Si localized in an outer shell with respect to Fe.

Our spatially resolved analysis shows that the EW of the Cr and Fe lines are correlated in the different regions of the remnant, with regions having the highest Fe abundances also showing the highest Cr EW. Theoretical models of delayed-

[6] *Chandra* data have been reprocessed with CIAO 4.7 and spectra have been extracted with the SPECEXTRACT script.

detonation show that besides the explosive Si-burning regime, different yields of Fe-group elements can be synthesized in incomplete Si-burning layers, depending on variations in the details of the transition from deflagration to detonation (e.g., Iwamoto et al. 1999). The indications of a spatial colocation of Fe and Cr which we obtained suggest that the bulk of the shocked Fe-group elements in Tycho's SNR have been synthesized in the explosive Si-burning regime (as in *Kepler*'s SNR, see Park et al. 2013).

We also found indications for the presence of Ti line emission, confirmed by the joint *Chandra* and *XMM-Newton* data analysis. We verified that this emission is concentrated in regions characterized by bright emission from Cr and Fe K. We then concluded that the spatial distribution of the Ti-rich ejecta should follow that of the Fe-rich ejecta in Tycho's SNR. This clearly suggests that Fe-peak nuclei are spatially colocated in the remnant, in agreement with the predictions of multi-D models of Type Ia SN explosions.

The *Swift/BAT* observations of radioactive emission from ^{44}Ti points toward a total mass $M_{44\mathrm{Ti}} > 10^{-5}\,M_{\odot}$ (Troja et al. 2014). This value is consistent with that expected from a delayed-detonation explosion, which appears to be particularly suited for Tycho's SNR (e.g., Badenes et al. 2006). Delayed-detonation models (e.g., Iwamoto et al. 1999) generally predict much larger yields of ^{48}Ti ($5-7\times10^{-4}\,M_{\odot}$) and ^{50}Ti ($\sim3\times10^{-4}\,M_{\odot}$) than ^{44}Ti. We thus expect these heavy isotopes to contribute predominantly to the X-ray line emission.

We can evaluate whether the observed Ti line flux reported in Table 1 is sound by comparing it to the flux of the Cr emission line. In particular, in region 1, we obtain a line flux ratio of the Ti to Cr emission lines of $N_{\mathrm{Ti}}/N_{\mathrm{Cr}} = 0.3 \pm 0.2$ (see Table 1). The expected line flux ratio of the Ti to Cr emission lines is $N_{\mathrm{Ti}}/N_{\mathrm{Cr}} \sim M_{\mathrm{Ti}}/M_{\mathrm{Cr}} \times E_{\mathrm{Ti}}/E_{\mathrm{Cr}}$, where $M_{\mathrm{Ti,Cr}}$ indicate the mass of the shocked (i.e., X-ray emitting) Ti and Cr, respectively, and $E_{\mathrm{Ti,Cr}}$ are the corresponding emissivities per ion. If we consider that Ti and Cr are spatially colocated, then we can assume that the ratio $M_{\mathrm{Ti}}/M_{\mathrm{Cr}}$ is the same as the ratio of the total (shocked and unshocked) masses of Ti to Cr synthesized at the explosion. This mass ratio is predicted to be $M_{\mathrm{Ti}}/M_{\mathrm{Cr}} \sim 0.06$ (Iwamoto et al. 1999). To derive the Ti and Cr emissivities, we adopt the same approach as Badenes et al. (2008a; see also Hwang et al. 2000) by interpolating the Kα emissivities of Si, S, Ar, Ca, Fe, and Ni for a plasma in non-equilibrium of ionization[7] having the best-fit temperature and ionization timescale that we obtained in region 1 for the high τ component (see Table 1), which is the one that mainly contribute to the line emission. We thus obtain $E_{\mathrm{Ti}}/E_{\mathrm{Cr}} \sim 2$. Therefore, the expected Ti to Cr line flux ratio is $N_{\mathrm{Ti}}/N_{\mathrm{Cr}} \sim 0.12$, which is consistent with that observed in region 1. Despite the large uncertainties involved, we conclude that the observed Ti flux appears to be reasonable and consistent with expectations.

Further observations are necessary to study in detail the spatial distribution of the Ti-rich ejecta in Tycho's SNR. Hard X-ray observations performed with the *NuSTAR* telescope will allow us to trace the ^{44}Ti emission with high spatial resolution and to verify if it is consistent with that of the Fe K emission (shown in blue in Figure 1), as suggested by our analysis. However, we point out that the abundance of neutron-rich elements is highly sensitive to the electron captures taking place in the central layers of the exploding star, and so, in principle, the spatial distributions of ^{48}Ti and ^{50}Ti may not coincide with that of the radioactive ^{44}Ti (though an efficient mixing is expected).

A major leap forward will be provided by the next generation of X-ray telescopes. As an example, we simulated an 80 ks observations of the Fe-rich region of Tycho's SNR, performed with the Soft X-ray Spectrometer of the forthcoming *Astro-H* mission (Takahashi et al. 2014 and references therein). We verified that it will be possible to detect the Ti line in the whole field of view of the telescope with a very high statistical confidence (5σ). A detailed study of the spatial distribution of the shocked Ti will be possible with the *Athena* telescope (Decourchelle et al. 2013; Nandra et al. 2013). We simulated a 50 ks observation of Tycho's SNR performed with *Athena* X-IFU (Ravera et al. 2014) and found that by assuming an average line flux equal to that observed in region 1, the X-IFU spectra will allow us to detect the Ti emission line in 1 arcmin^2 regions at more than 5σ.

We thank the anonymous referee for comments and suggestions. This paper was partially funded by the PRIN INAF 2014 grant. M.M. thanks M. Dadina for discussions about the X-IFU instrumental background.

[7] We have used the ATOMDB database and the APEC non-equilibrium ionization library Libapecnei, see http://www.atomdb.org/index.php.

REFERENCES

Badenes, C., Borkowski, K. J., Hughes, J. P., Hwang, U., & Bravo, E. 2006, ApJ, 645, 1373
Badenes, C., Bravo, E., & Hughes, J. P. 2008a, ApJL, 680, L33
Badenes, C., Hughes, J. P., Cassam-Chenaï, G., & Bravo, E. 2008b, ApJ, 680, 1149
Bykov, A. M., Ellison, D. C., Osipov, S. M., Pavlov, G. G., & Uvarov, Y. A. 2011, ApJL, 735, L40
Cassam-Chenaï, G., Hughes, J. P., Ballet, J., & Decourchelle, A. 2007, ApJ, 665, 315
Chiotellis, A., Kosenko, D., Schure, K. M., Vink, J., & Kaastra, J. S. 2013, MNRAS, 435, 1659
Decourchelle, A., Costantini, E., Badenes, C., et al. 2013, arXiv:1306.2335
Eriksen, K. A., Hughes, J. P., Badenes, C., et al. 2011, ApJL, 728, L28
Gamezo, V. N., Khokhlov, A. M., & Oran, E. S. 2005, ApJ, 623, 337
Grefenstette, B. W., Harrison, F. A., Boggs, S. E., et al. 2014, Natur, 506, 339
Hwang, U., Decourchelle, A., Holt, S. S., & Petre, R. 2002, ApJ, 581, 1101
Hwang, U., Hughes, J. P., & Petre, R. 1998, ApJ, 497, 833
Hwang, U., Petre, R., & Hughes, J. P. 2000, ApJ, 532, 970
Iwamoto, K., Brachwitz, F., Nomoto, K., et al. 1999, ApJS, 125, 439
Kasen, D., Röpke, F. K., & Woosley, S. E. 2009, Natur, 460, 869
Kramida, A., Y. Ralchenko, Reader, J., & NIST ASD Team 2014, NIST Atomic Spectra Database (ver. 5.2, Gaithersburg, MD: NIST http://physics.nist.gov/asd)
Krause, O., Tanaka, M., Usuda, T., et al. 2008, Natur, 456, 617
Miceli, M., Decourchelle, A., Ballet, J., et al. 2006, A&A, 453, 567
Miceli, M., Orlando, S., Reale, F., Bocchino, F., & Peres, G. 2013, MNRAS, 430, 2864
Morlino, G., & Caprioli, D. 2012, A&A, 538, A81
Nandra, K., Barret, D., Barcons, X., et al. 2013, arXiv:1306.2307
Nomoto, K., Thielemann, F.-K., & Yokoi, K. 1984, ApJ, 286, 644
Orlando, S., Bocchino, F., Miceli, M., Petruk, O., & Pumo, M. L. 2012, ApJ, 749, 156
Park, S., Badenes, C., Mori, K., et al. 2013, ApJL, 767, L10
Ravera, L., Barret, D., den Herder, J. W., et al. 2014, SPIE Proc., 9144, 2
Röpke, F. K., & Hillebrandt, W. 2005, A&A, 431, 635
Seitenzahl, I. R., Ciaraldi-Schoolmann, F., Röpke, F. K., et al. 2013, MNRAS, 429, 1156
Slane, P., Lee, S.-H., Ellison, D. C., et al. 2014, ApJ, 783, 33
Takahashi, T., Mitsuda, K., Kelley, R., et al. 2014, arXiv:1412.2351
Tamagawa, T., Hayato, A., Nakamura, S., et al. 2009, PASJ, 61, 167

Tanaka, M., Mazzali, P. A., Stanishev, V., et al. 2011, MNRAS, 410, 1725
Troja, E., Segreto, A., la Parola, V., et al. 2014, arXiv:1411.0991
van Paradijs, J., & Bleeker, J. A. M. (ed.) 1999, X-Ray Spectroscopy in Astrophysics, Vol. 520 (Berlin: Springer)
Vancura, O., Gorenstein, P., & Hughes, J. P. 1995, ApJ, 441, 680
Wang, L., Baade, D., Höflich, P., & Wheeler, J. C. 2003, ApJ, 592, 457
Wang, L., Baade, D., Höflich, P., et al. 2006, ApJ, 653, 490
Wang, W., & Li, Z. 2014, ApJ, 789, 123
Williams, B. J., Borkowski, K. J., Ghavamian, P., et al. 2013, ApJ, 770, 129
Yamaguchi, H., Badenes, C., Petre, R., et al. 2014, ApJL, 785, L27
Yang, X. J., Tsunemi, H., Lu, F. J., et al. 2013, ApJ, 766, 44